Title

Structural pathway for allosteric activation of the autophagic PI 3-kinase complex I

Journal

Proceedings of the National Academy of Sciences of the United States of America, 116(43)

ISSN

0027-8424

Authors

Young, Lindsey N

Goerdeler, Felix

Hurley, James H

Publication Date

2019-10-22

DOI

10.1073/pnas.1911612116

Peer reviewed

Structural pathway for allosteric activation of the autophagic PI 3-kinase complex I

Lindsey N. Young[a,b,c,1], Felix Goerdeler[a,2], and James H. Hurley[a,b,c,3]

[a]Department of Molecular and Cell Biology, University of California, Berkeley, CA 94720; [b]California Institute for Quantitative Biosciences, University of California, Berkeley, CA 94720; and [c]Molecular Biophysics and Integrated Bioimaging Division, Lawrence Berkeley National Laboratory, Berkeley, CA 94720

Edited by Axel T. Brunger, Stanford University, Stanford, CA, and approved September 18, 2019 (received for review July 6, 2019)

Autophagy induction by starvation and stress involves the enzymatic activation of the class III phosphatidylinositol (PI) 3-kinase complex I (PI3KC3-C1). The inactive basal state of PI3KC3-C1 is maintained by inhibitory contacts between the VPS15 protein kinase and VPS34 lipid kinase domains that restrict the conformation of the VPS34 activation loop. Here, the proautophagic MIT domain-containing protein NRBF2 was used to map the structural changes leading to activation. Cryoelectron microscopy was used to visualize a 2-step PI3KC3-C1 activation pathway driven by NRFB2 MIT domain binding. Binding of a single NRBF2 MIT domain bends the helical solenoid of the VPS15 scaffold, displaces the protein kinase domain of VPS15, and releases the VPS34 kinase domain from the inhibited conformation. Binding of a second MIT stabilizes the VPS34 lipid kinase domain in an active conformation that has an unrestricted activation loop and is poised for access to membranes.

autophagy | cryo-EM | lipid kinase

Autophagy is a core cellular process, conserved throughout eukaryotes, which is the central recycling system for the removal of misfolded proteins, damaged organelles, and the recycling of nutrients in starvation. Autophagic dysfunction is implicated in many disease states, including neurodegeneration, immune disorders, cancer, and aging, among others (1). The class III phosphatidylinositol-3 kinase complexes (PI3KC3) I and II (PI3KC3-C1 and -C2), respectively, are essential for the initiation and expansion of autophagosomes (2–5). PI3KC3 generates the lipid phosphatidylinositol-3-phosphate, PI(3)P, which is recognized by the WIPI proteins. WIPIs, in turn, recruit the machinery that conjugates the autophagosomal marker LC3 to the expanding autophagosomal membrane (6). PI3KC3-C1 has been proposed to be a promising therapeutic target for autophagy activators (7) because the generation of PI(3)P is absolutely required for the recruitment of downstream autophagy proteins. There is considerable medical interest in selectively activating this pathway to promote human health and treat disease, yet there are no FDA-approved pharmaceuticals that uniquely activate autophagy.

PI3KC3-C1 consists of the lipid kinase VPS34, the putative serine/threonine protein kinase VPS15, the regulatory subunit BECN1, and the early autophagy-specific targeting subunit ATG14 (8, 9). In PI3KC3-C2, ATG14 is replaced with UVRAG (10), while the other 3 subunits are preserved. The overall architecture of both PI3KC3-C1 and -C2 has the shape of the letter V (11, 12) (Fig. 1*A*). The long coiled coils of BECN1 and ATG14 scaffold the left arm in the standard view, with the membrane binding BARA domain of BECN1 located at the outermost tip of the arm. PI3KC3-C2 is inhibited by Rubicon and the HIV-1 protein Nef (13–15), which regulate membrane docking by the tip of the left arm. The catalytic domains of the kinases VPS34 and VPS15 are at the tip of the right arm (11, 12). PI3KC3 complexes are phosphoregulated by the Unc-51 like autophagy-activating kinase 1 (ULK1) complex (16), among other kinases (3). PI3KC3-C1 is inhibited by anti-apoptotic proteins Bcl-2/Bcl-XL (10). The binding of Bcl-2/Bcl-XL and the best-characterized phosphoregulatory modulations of PI3KC3-C1 map to the base of the V. Thus far, the structural mechanisms of the many PI3KC3 regulators acting at the base of the V have been undefined.

Nuclear Receptor Binding Factor 2 (NRBF2) is a positive regulator of PI3KC3-C1 that also acts at the base of the V shape (17). NRBF2 was identified as a PI3KC3-C1–associated factor through proteomics of the mammalian autophagy network (18). Depletion of NRBF2 reduced autophagosome formation, implicating NRBF2 as proautophagic (18). Work in *Saccharomyces cerevisiae* identified Atg38 as the homolog of NRBF2 and confirmed Atg38 to be a proautophagic component of PI3KC3-C1 (19). The proautophagic function of NRBF2 has been confirmed by most reports in mammalian cells (20–24), although contrary findings were reported by one group (24). NRBF2 and its ortholog Atg38 contain an N-terminal Microtubule Interacting and Trafficking (MIT) domain that binds to PI3KC3-C1, followed by a central dimeric coiled-coil domain (17, 19, 25) (Fig. 1*B*). Dimerization can be decoupled from activation, as the N-terminal MIT domain ($NRBF2^{MIT}$) alone is sufficient to enhance the kinase activity of the autophagy-specific PI3-Kinase in vitro (17) and to rescue autophagy induction in MEFs (21). Here, we used cryoelectron microscopy (cryo-EM) and

Significance

Autophagy is a prosurvival pathway of cellular self-consumption that is essential for the homeostasis of eukaryotic cells. Understanding the switching of autophagy on and off at the structural level has been a major goal in autophagy research. The active state structure is poorly stable and has until now not been possible to crystallize or to reconstruct by cryoelectron microscopy. We now provide a structure of the autophagy-initiating phosphatidylinositol 3-kinase (PI3K) lipid kinase complex I in the activated state. The structure shows how rearrangements in the right arm of the complex triggered by NRBF2 lead the lipid kinase domain to move to a geometry with an unrestricted activation loop and an active site poised to phosphorylate membrane-embedded phosphatidylinositol (PI).

Author contributions: L.N.Y. and J.H.H. designed research; L.N.Y. and F.G. performed research; L.N.Y. and J.H.H. analyzed data; and L.N.Y. and J.H.H. wrote the paper.

Competing interest statement: J.H.H. is a scientific founder of, and receives research funding from, Casma Therapeutics.

This article is a PNAS Direct Submission.

Data deposition: The EM density maps have been deposited in the Electron Microscopy Data Bank (EMDB), https://www.ebi.ac.uk/pdbe/emdb (accession no. EMDB-20387, MIT-Fusion cryoEM map, mask for refinement, and FSC curve; accession no. EMDB-20390, activated PI3KC3-C1 and full-length NRBF2 cryo-EM map, mask used for refinement, and FSC curve).

[1]Present address: Division of Biological Sciences, University of California San Diego, La Jolla, CA 92161.

[2]Present address: Department of Biochemistry, Freie Universität Berlin, 14195 Berlin, Germany.

[3]To whom correspondence may be addressed. Email: jimhurley@berkeley.edu.

This article contains supporting information online at www.pnas.org/lookup/suppl/doi:10.1073/pnas.1911612116/-/DCSupplemental.

First published October 7, 2019.

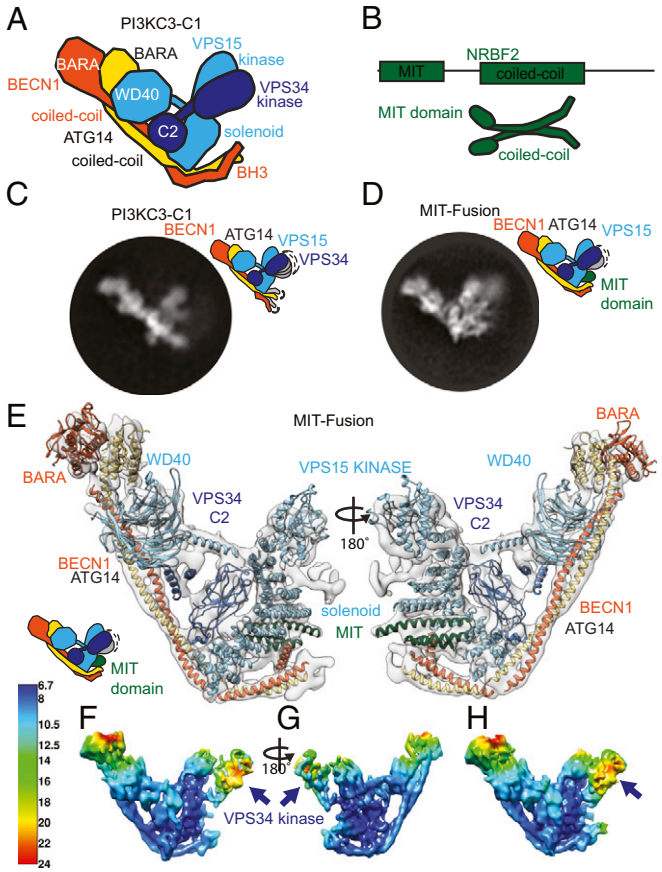

Fig. 1. Cryo-EM structure of "MIT-Fusion" (BECN1-NRBF2^{MIT} PI3KC3-C1). (*A*) Schematic of PI3KC3-C1 containing VPS34, VPS15, BECN1, and ATG14. (*B*) Schematic of NRBF2. (*C*) Two-dimensional cryo-EM class average of PI3KC3-C1 for comparison, illustrating the mobility of the VPS34 kinase domain. (*D*) Two-dimensional cryo-EM class average of MIT-Fusion. (*E*) Cryo-EM reconstruction of MIT-Fusion with VPS34 helical and catalytic domains masked out. Models originate PDB depositions for yeast PI3KC3-C2 (5DFZ), NRBF2^{MIT} (4ZEY), and BECN1^{BARA} (4DDP). The cryo-EM map has been deposited in the EMDB under accession no. EMDB-20387 (34). (*F*) Local resolution of MIT-Fusion structure with VPS34 helical and kinase domains included in masking, shown at a contour level of 10 σ or 0.0097 in Chimera and rotated 180° in *G*. (*H*) The VPS34 catalytic domain is visible (arrow), albeit at a low resolution of 18–24 Å, when contoured at a threshold of 6 σ or 0.0058 in Chimera.

allied methods to show how NRBF2 allosterically activates PI3KC3-C1 at a structural and mechanistic level.

Results

Characterization of PI3KC3-C1 Containing a NRBF2-MIT-BECN1 Fusion Construct. We had previously found that (*i*) the isolated NRBF2^{MIT} was sufficient to activate PI3KC3-C1, and (*ii*) that the principal binding site of NRBF2^{MIT} included the N-terminal domain of BECN1 (17). In order to generate a nondissociable NRBF2^{MIT} complex with PI3KC3-C1 for cryo-EM studies, we built on these observations by fusing NRBF2^{MIT} to the N terminus of BECN1 using a flexible (Gly-Gly-Ser)$_4$ linker (*SI Appendix*, Fig. S1 *A* and *B*). To confirm that the MIT-linker construct occupies the same binding site within PI3KC3-C1 as unfused NRBF2, we purified a variant PI3KC3-C1 in which WT BECN1 was replaced by NRBF2^{MIT}-BECN1 ("MIT-Fusion"), performed HDX-MS, and compared the HDX protection of the NRBF2 complex to the fusion. In both cases, the reference was taken as WT PI3KC3-C1 in the absence of NRBF2 (*SI Appendix*, Fig. S1*C*).

We observed protection patterns in VPS34, BECN1, ATG14, and VPS15 consistent with NRBF2 binding near the base of the complex (*SI Appendix*, Fig. S1 *D–G*). Peptides within the N-terminal domains of BECN1 and ATG14, the VPS15 helical solenoid, and the VPS34 C2 domain showed HDX decreases of up to 50%. However, most HDX decreases throughout the remainder of the 4 subunits did not exceed ~10%. In the NRBF2–BECN1 fusion complex, the regions that showed the highest protection were typically even more protected (*SI Appendix*, Fig. S1 *D–G*). Two regions of ATG14 that were ~15% protected in the NRBF2 complex were ~30% protected in the fusion, for example (*SI Appendix*, Fig. S1*F*). Therefore, the presence of the fused NRBF2^{MIT} generally recapitulates the qualitative protection pattern seen in the noncovalent complex with intact NRBF2, but the degree of protection is greater. This is presumably because the fused complex cannot dissociate when it is diluted into D_2O for exchange experiments. Outside of the regions expected to interact with NRBF2, increased protection was also noted. For example, most of the catalytic domains of VPS34 and VPS15 manifested a ~20% increase in protection in the fusion (*SI Appendix*, Fig. S1 *D* and *G*). These increases are suggestive of a more global decrease in protein dynamics in the fused construct.

Cryo-EM Structure of the BECN1–MIT–Fusion Complex. Previous EM analyses of PI3KC3s have been limited by the dynamic character of these complexes and by their tendency to be in preferred orientations on EM grids (11, 17, 25, 26). Even when preferred orientations can be reduced or eliminated, the dynamics of the catalytic right arm of the complex (27) has still limited analysis (14). The apparent reduction in dynamics in the BECN1-NRBF2^{MIT} form of PI3KC3-C1 suggested that this sample might be more tractable to cryo-EM than the WT PI3KC3-C1 and -C2 complexes. Two-dimensional class averages of BECN1-NRBF2^{MIT} PI3KC3-C1 showed additional features compared to WT PI3KC3-C1 (Fig. 1 *C* and *D*). A reconstruction was obtained with an overall resolution of 7.7 Å and local resolution ranging from 6.7 to 24 Å (Fig. 1 *E* and *F* and *SI Appendix*, Fig. S2 and Table S1), showing the expected V-shaped architecture. Domains were flexibly fitted by taking the crystal structures of yeast PI3KC3-C2 (12) and the NRBF2^{MIT} (Protein Data Bank [PDB] ID code 4ZEY) as the starting point (Fig. 1*E*). Despite the lack of side-chain definition at the attained resolution, it was possible to dock the NRBF2^{MIT} into density unambiguously on the basis of the unequal lengths of the 3 MIT helices.

Density for the catalytic domains at the tip of the right arm is less defined than for the rest of the structure; however, the density was clear enough to show that the VPS15 kinase is displaced relative to its position in the yeast PI3KC3-C2 structure. In contrast, the VPS34 lipid kinase domain was difficult to visualize. Extensive efforts were made to refine a 3D structural class containing hints of VPS34 kinase density, yet even after winnowing over 10^6 particles to a set of ~20,000 (*SI Appendix*, Fig. S2), the density for the VPS34 kinase domain was of marginal quality. This density was visualized only when the contour level was lowered to 6 σ, as compared to the rest of the structure, which was evident at a contour level of 10 σ. Even then, local resolution was lower in the VPS34 kinase domain (16–24 Å) as compared to 6.7–10 Å for the structural core. In the larger ensemble of 3D classes as shown in *SI Appendix*, Fig. S2, density for the VPS34 kinase is completely missing. We conclude that the presence of a single NRBF2 MIT domain is insufficient for fully ordered engagement of the VPS34 kinase domain with the rest of the complex.

The NRBF2 MIT is localized near the base of the right arm, on the back side of the complex in the standard view (Fig. 1*E*). The extended contacts seen with multiple subunits are consistent with the high affinity (40 nM) of NRBF2 for PI3KC3-C1 (17). The MIT interacts extensively with the central part of the VPS15 helical solenoid. The MIT also interacts with a helical density associated with the N-terminal portions of BECN1 and ATG14 (Fig. 1*E*). On the basis of its high HDX protection (*SI Appendix*, Fig. S1*E*), this helix was provisionally assigned as the BH3 domain of

BECN1. This region has not previously been visualized in any of the PI3KC3 structures, and it therefore appears to become ordered only in the presence of NRBF2^{MIT}. This helix in turn interacts with the most N-terminal portions of the parallel BECN1 and ATG14 coiled coils (Fig. 1*E*).

Activation Requires NRBF2^{MIT} Binding at 2 Sites. The isolated NRBF2^{MIT} domain, added at a 60-fold molar excess to PI3KC3-C1, enhanced lipid kinase activity to the same degree as the full-length dimeric NRBF2 (Fig. 2*A*) (17). Given that observation and the apparent full occupancy of the MIT binding site in the cryo-EM structure, we had expected that the BECN1-NRBF2^{MIT} fusion C1 complex would also have enhanced activity. Contrary to expectations, the BECN1-NRBF2^{MIT} fusion C1 complex had essentially the same activity as the C1 complex in the absence of NRBF2 (Fig. 2*A*). Addition of NRBF2^{MIT} to the BECN1-NRBF2^{MIT} fusion C1 complex enhanced activity to a similar extent as for the WT complex (Fig. 2*A*). We interpret this to mean that activation of PI3KC3-C1 by NRBF2 requires NRBF2^{MIT} to engage with at least 2 distinct binding sites on PI3KC3-C1.

In order to directly test the existence of a second MIT binding site, negative stain (NS) EM was carried out for the BECN1-NRBF2^{MIT} fusion C1 in the presence of a maltose binding protein (MBP)-tagged NRBF2^{MIT} construct. Two-dimensional class averages of NS-EM images showed that a second copy of NRBF2^{MIT} binds to the MIT–Fusion complex as shown by the extra density for the MBP-tagged NRBF2^{MIT} (Fig. 2*B*). This extra density is located at the base of the complex near the first binding site, suggesting that both N-terminal MIT domains of a single full-length dimeric NRBF2 can occupy both sites simultaneously. These data suggest that the second binding site is lower affinity than the first, and that both binding sites are required for enzymatic activation.

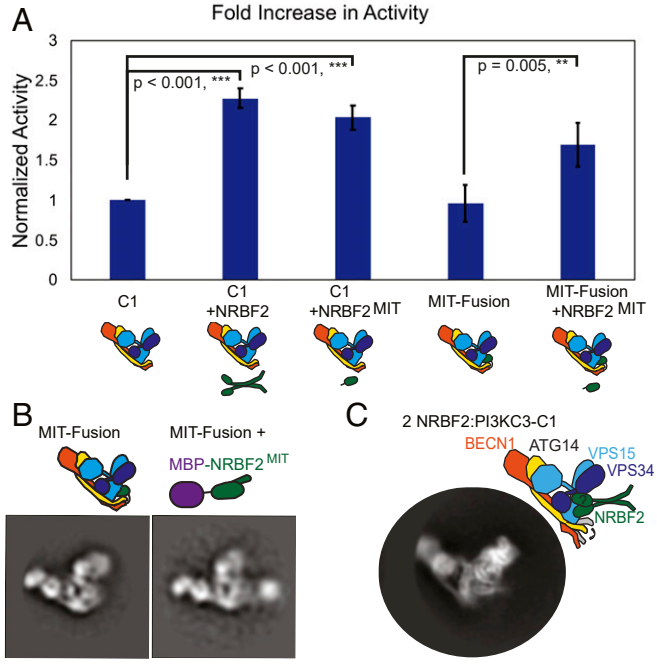

Fig. 2. Two copies NRBF2^{MIT} are required for activation. (*A*) Activity assay of PI3KC3-C1 and MIT-Fusion, with or without NRBF2^{MIT} or NRBF2. The average of 3 experiments performed in duplicate and normalized to PI3KC3-C1 activity are shown. The error bars represent the SEM, and *P* values were determined between PI3KC3-C1 and NRBF2^{MIT} or NRBF2, and MIT-Fusion and NRBF2. (*B*) Negative stain 2D class average of MIT-Fusion and MIT-Fusion incubated with MBP- NRBF2^{MIT}. (*C*) Two-dimensional cryo-EM class average of full-length NRBF2 bound to PI3KC3-C1.

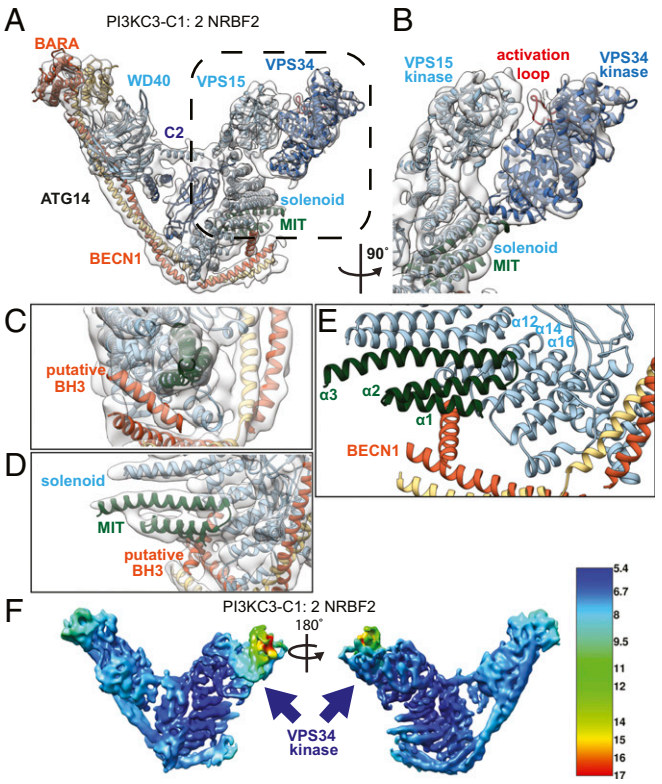

Fig. 3. CryoEM structure containing PI3KC3-C1 and full-length, dimeric NRBF2. (*A*) Cryo-EM reconstruction of a sample containing PI3KC3-C1 and full-length NRBF2 (PI3KC3-C1:2NRBF2) contoured at 10 σ or 0.0144 in Chimera. The cryo-EM map has been deposited in the EMDB under accession no. EMDB-20390 (35). Models docked into cryo-EM reconstruction include yeast PI3KC3-C2 (5DFZ), VPS34 kinase domain (4PH4), NRBF2^{MIT} (4ZEY), and BECN1^{BARA} (4DDP). (*B*) Close-up of the cryo-EM reconstruction of the VPS15 kinase (cyan, PDB ID code 5DFZ) and VPS34 kinase domains (blue, PDB ID code 4PH4), activation loop of VPS34 in red. (*C*) Close-up of the cryoEM reconstruction for the regions contacting NRBF2^{MIT} (red) include density for a helix, putatively, the BH3 helix of BECN1 (orange). (*D*) Close-up of solenoid of VPS15 (cyan) ,which provides an extensive face for MIT binding. (*E*) Cartoon representation of α-helices-1, 2, 3 of NRBF2^{MIT} contacting α-helices 12, 14, 16 of the VPS15 solenoid as well as the putative BH3 helix. (*F*) Local resolution estimates for PI3KC3:2NRBF2, with the VPS34 catalytic domain defined at 8–18 Å resolution (arrow).

Cryo-EM Structure of Full-Length NRBF2 Bound to PI3KC3-C1. A cryo-EM dataset was obtained for PI3KC3-C1 bound to full-length NRBF2. Two-dimensional class averages showed additional ordered features at the base of the complex and on the right arm as compared to the MIT fusion (Fig. 2*C*). Single-particle reconstruction was carried out to an overall resolution of 6.6 Å (Fig. 3 *A–E* and *SI Appendix*, Fig. S3 and Table S1), with local resolution ranging from 5.4 to 18 Å (Fig. 3*F*). The position of the first NRBF2^{MIT} is essentially identical to that seen in the MIT fusion. The local resolution of the NRBF2^{MIT} is improved, enabling the MIT 3-helix bundle to be placed with greater precision (Fig. 3 *C–E*). The structure shows the N terminus of MIT α1, the α2-α3 connector, and the length of α3 of NRBF2^{MIT} with helices α12, α14, and α16 of the VPS15 solenoid (Fig. 3*E*).

The VPS34 kinase domain in the NRBF2 complex is better ordered than in the MIT fusion, the major point of difference between the 2. The VPS34 kinase is fully visible at the same 10 σ contour level as the rest of the structure, although less ordered as measured by local resolution (Fig. 3*F*). Although most of the kinase domain is at ∼8-Å resolution (Fig. 3*F*), the most distal portions are as low as 18-Å resolution. Despite indications of additional features and what appears to be the coiled-coil stalk

of dimeric NRBF2 projecting away from the right arm in the 2D class averages (Fig. 2*C*), it was not possible to assign the locations of these moieties definitively to the density features at the periphery of the VPS34 kinase domain. We infer that the second NRBF2^{MIT} is bound to this relatively flexible region, and it is not surprising that small domains associated with mobile portions of a complex would not be evident.

Comparison to Inactive Conformation of PI3KC3-C2. In the yeast crystal structure, the VPS15 kinase domain contacts the activation loop of VPS34 such that VPS15 inhibits basal VPS34 activity (12) (Fig. 4 *A*–*C*). Binding of the first NRBF2^{MIT} to the VPS15 solenoid alters its bend such that changes are propagated to the N terminus of the solenoid where it meets the VPS15 kinase domain (Fig. 4 *A* and *B*). This change pushes the N-terminal part of the solenoid in the outward direction relative to the base of the V. This, in turn, pushes the VPS15 kinase away from the VPS34 kinase by ~10 Å near to solenoid and ~20 Å at the tip (Fig. 4*B*). This movement of VPS15 breaks the inhibitory contacts with the VPS34 activation loop (Fig. 4*D*). This triggers the final change in the series, a 25° pivot of VPS34 about the base of the kinase domain such that the distal tip of the kinase domain moves 45 Å (Fig. 4*D*). These changes separate the 2 domains so that the gap between the most C-terminal ordered residue of VPS34 and the N-terminal residue of VPS15 increases from 28 to 51 Å (Fig. 4 *C* and *D*). This change completely liberates the VPS34 kinase activation loop seen in the inactive structure.

Discussion

The ultimate goal of structural studies of PI3KC3 complex is to understand how they are switched on and off in autophagy by phosphoregulation and by binding of regulatory factors such as Bcl-2, Ambra1, Rubicon, and NRBF2. The structure of one PI3KC3 complex, yeast PI3KC3-C2, has been determined in an

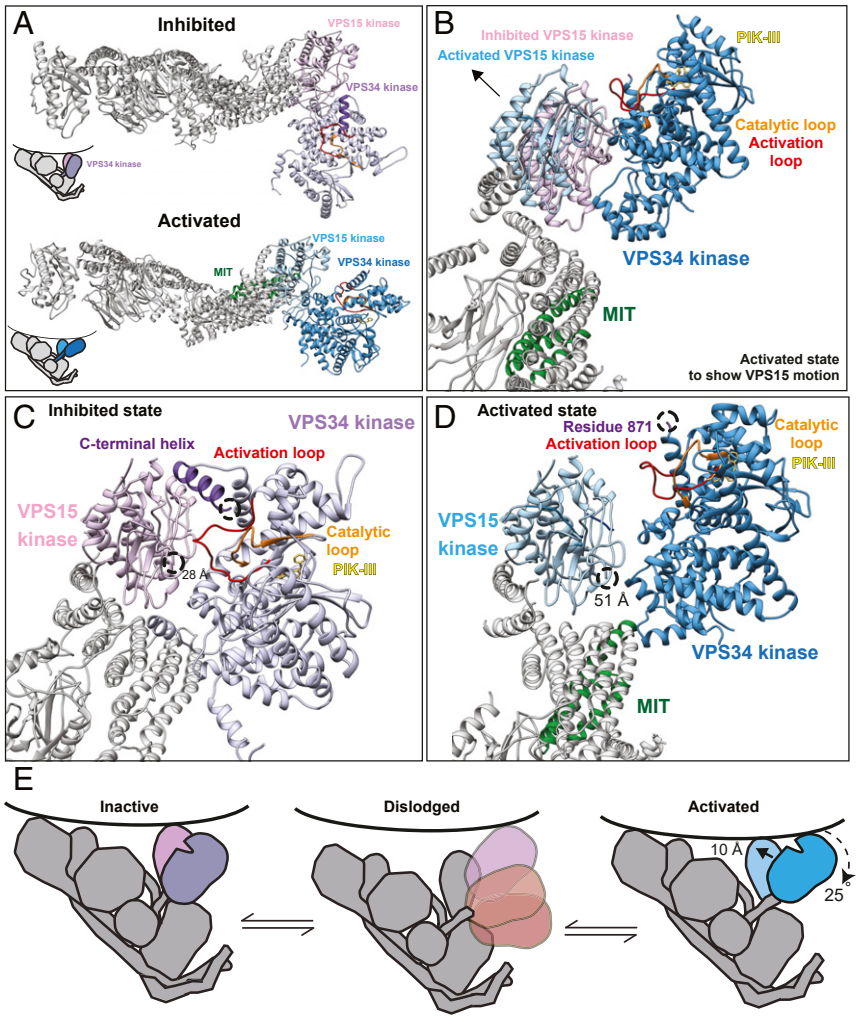

Fig. 4. Activation mechanism for transitioning PI3KC3-C1 from its inhibited to its activated state. (*A*) Top-down view of the inhibited PI3KC3-C1 (yeast PI3KC3-C2, 5DFZ) state, the VPS34 kinase domain sits perpendicular to VPS15. Top-down view of the activated PI3KC3-C1 (models from PDB ID codes 5DFZ, 4PH4, 4ZEY, 4DDP) state docked into the cryo-EM reconstruction (EMDB-20390) (35), the VPS15 kinase domain shifts by 10 Å to come more in line with rest of the complex. While VPS34 pivots 25°, the base of the VPS34 kinase domain moves by 5 Å while the top moves by 45 Å. (*B*) The inhibited state (pink) of VPS15 moves 10 Å away from VPS34 (blue) to reach its activated state (cyan), exposing the activation loop (red) of VPS34. (*C*) In the inhibited state, the activation loop (red) of VPS34 (lavender, from inhibited state 5DFZ) is occluded by the VPS15 kinase domain (pink, PDB ID code 5DFZ). (*D*) In the activated state, the activation loop (red) of VPS34 (blue) is released from VPS15 (cyan) inhibition and is more available to engage substrate. (*E*) Activation model of PI3KC3-C1 on membranes, in the inhibited state, the activation loop of VPS34 is not in a position to engage substrate. In solution, PI3KC3-C1 is highly dynamic, and the VPS34 kinase domain can dislodge (light pink) from the complex to directly bind membranes without the benefit of the rest of the complex. In the activated state, VPS34 is positioned in a precise geometry such that the activation loop of VPS34 is accessible to substrate in the membrane.

inactive conformation (12). The kinase domain of VPS15 keeps basal activity low by restricting the activation loop of VPS34 (12). Our laboratory previously found that the VPS34 kinase domain is highly dynamic (11, 27). We found that "leashing" the VPS34 kinase domain to the VPS15 kinase domain with a 12-residue linker blocked even basal kinase activity (27). This showed that a substantial structural change relative to the published PI3KC3-C2 conformation was essential for any activity, yet the precise nature of the structural change was not clear. The structural change here involves an increase in the VPS34-C to VPS15-N gap from 28 to 51 Å. The increase in distance on activation is great enough that it would be prevented by a 12-amino acid linker. The structural change observed here is thus sufficient to account for the phenotype of the leashed construct.

NRBF2 was chosen as the model allosteric regulator of PI3KC3 in this study because it is one of the well-established protein activators of PI3KC3-C1. By using NRBF2 as a structural probe, it has now been possible to visualize conformational changes likely to be associated with multiple regulatory mechanisms. The base of the complex, near the first MIT binding site, is where a number of posttranslational and regulatory signals converge on the autophagic-specific PI3KC3-C1 via the regulatory hub, the N termini of BECN1 and ATG14 (3). This is the site that is modulated by ULK1, AMPK, and Bcl-2, among prominent positive and negative regulators. A single ordered helix is visualized bound to NRBF2^{MIT}, which we provisionally assigned as the BECN1 BH3 domain, because the BH3 domain is the portion of BECN1 which is most protected from HDX upon NRBF2 binding. The BH3 is also the binding site for the PI3KC3 inhibitor Bcl-2, suggesting there could be some interplay between regulation by Bcl-2 and NRBF2. The proximity of the BECN1 and ATG14 N-terminal domains to NBRF2 MIT and to the conformationally labile VPS15 solenoid suggest that other N-terminal interactors and posttranslational modifications could also act through the NRBF2 binding site and so communicate with the most distant VPS34 lipid kinase domain.

Full-length NRBF2 can dimerize PI3KC3-C1, forming a dimer of pentamers (17, 25), while full-length Atg38 does not show this dimerizing effect with respect to yeast PI3KC3-C1 (25). We previously hypothesized that full-length NRBF2 could tether 2 copies of PI3KC3-C1 within the cell, perhaps facilitating vesicle tethering or membrane-binding interactions. The finding that 2 copies of NRBF2^{MIT} are necessary for full PI3KC3-C1 activation argues that the activating mode of binding is probably 1 NRBF2 dimer per PI3KC3-C1 complex, which is incompatible with the C1 dimerization model. One remaining uncertainty is the location of the binding site for the second NRBF2 MIT domain, which we have been unable to visualize, probably due to the mobility of the region of the PI3KC3-C1 complex involved.

NRBF2 (and yeast Atg38) are specific for PI3KC3-C1 and, thus, specific for autophagy initiation. Our previous HDX-MS work and the cryo-EM work shown here, however, did not show evidence of direct contacts with the C1-unique subunit ATG14. The position of the NRBF2 MIT overlaps with the UVRAG C2 domain in the structure (*SI Appendix*, Fig. S4). This suggests that the presence of the UVRAG C2 domain is a main factor preventing NRBF2 from binding to PI3KC3-C2.

PI3KC3 complex structures have now been determined with the VPS34 catalytic domain in stable active and inactive conformations. The VPS34 catalytic domain is also capable of dislodging from the rest of the complex and sampling a wide range of conformations (11). We speculate that dislodging could facilitate the transition between the active and inactive conformations. The activity of the dislodged state appears to be intermediate between that of the stable inactive and active states (Fig. 4*E*). As judged by the phenotype of the leashed complex (27), the stable inactive conformation has almost no enzyme activity. The activity of the dislodged state seems likely to reflect that of the isolated VPS34 kinase domain, which is about ~10% of that of PI3KC3-C1 (27). The presence of a single NRBF2 MIT domain appears sufficient to block the stable inactive conformation, but insufficient to drive full occupancy of the stable active conformation. By contrast, both MIT domains together not only block the stable inactive conformation, they also promote high occupancy of the stable active structure. In this structure, not only are the catalytic site, the C-terminal membrane binding helix, and the activation loop of VPS34 unrestricted, but they are also presented to the membrane substrate with an ideal geometry for PI headgroup phosphorylation.

Materials and Methods

Human PI3KC3-C1 complexes containing the NRBF2 MIT-BECN1 fusion or an NRBF2 dimer were expressed in HEK293 cells, purified, and analyzed by cryo-EM (28–33). The structures were compared to each other and to the previously determined crystal structure of the inactive yeast PI3KC3-C2 complex (12). Fitting of the cryoEM maps was performed using homology models. Samples of PI3KC3-C1 MIT-Fusion and MIT-Fusion:MBP-NRBF2^{MIT} samples were analyzed by negative stain EM. HDX-MS experiments were performed on PI3KC3-C1, PI3KC3-C1 MIT-BECN1, and PI3KC3-C1:NRBF2. An average of 3 lipid kinase assays performed in duplicate and normalized to PI3KC3-C1 activity were carried out using the ADP-kinase Glo kit (Promega), with the error bars representing the SEM and *P* values determined using a Tukey comparison.

ACKNOWLEDGMENTS. We thank D. Toso, P. Tobias, and P. Grob for cryo-EM support and members of the University of California, Berkeley cryo-EM supergroup for helpful discussions. This research was supported by NIH Grants P01 GM051487 (to J.H.H.), R01 GM111730 (to J.H.H.), and F99 CA223029 (to L.N.Y.) and the Bakar Fellows Program (J.H.H.).

1. B. Levine, G. Kroemer, Biological functions of autophagy genes: A disease perspective. *Cell* **176**, 11–42 (2019).
2. J. M. Backer, The intricate regulation and complex functions of the Class III phosphoinositide 3-kinase Vps34. *Biochem. J.* **473**, 2251–2271 (2016).
3. J. H. Hurley, L. N. Young, Mechanisms of autophagy initiation. *Annu. Rev. Biochem.* **86**, 225–244 (2017).
4. Y. Ohashi, S. Tremel, R. L. Williams, VPS34 complexes from a structural perspective. *J. Lipid Res.* **60**, 229–241 (2019).
5. B. Bilanges, Y. Posor, B. Vanhaesebroeck, PI3K isoforms in cell signalling and vesicle trafficking. *Nat. Rev. Mol. Cell Biol.* **20**, 515–534 (2019).
6. H. C. Dooley *et al.*, WIPI2 links LC3 conjugation with PI3P, autophagosome formation, and pathogen clearance by recruiting Atg12-5-16L1. *Mol. Cell* **55**, 238–252 (2014).
7. L. Galluzzi, J. M. Bravo-San Pedro, B. Levine, D. R. Green, G. Kroemer, Pharmacological modulation of autophagy: Therapeutic potential and persisting obstacles. *Nat. Rev. Drug Discov.* **16**, 487–511 (2017).
8. K. Obara, T. Sekito, Y. Ohsumi, Assortment of phosphatidylinositol 3-Kinase complexes — Atg14p directs association of complex I to the pre-autophagosomal structure in Saccharomyces cerevisiae. *Mol. Biol. Cell* **17**, 1527–1539 (2006).
9. E. Itakura, C. Kishi, K. Inoue, N. Mizushima, Beclin 1 forms two distinct phosphatidylinositol 3-kinase complexes with mammalian Atg14 and UVRAG. *Mol. Biol. Cell* **19**, 5360–5372 (2008).
10. C. Liang *et al.*, Autophagic and tumour suppressor activity of a novel Beclin1-binding protein UVRAG. *Nat. Cell Biol.* **8**, 688–699 (2006).
11. S. Baskaran *et al.*, Architecture and dynamics of the autophagic phosphatidylinositol 3-kinase complex. *Elife***3**, e05115 (2014).
12. K. Rostislavleva *et al.*, Structure and flexibility of the endosomal Vps34 complex reveals the basis of its function on membranes. *Science* **350**, aac7365 (2015).
13. S. Pattingre *et al.*, Bcl-2 antiapoptotic proteins inhibit Beclin 1-dependent autophagy. *Cell* **122**, 927–939 (2005).
14. C. Chang *et al.*, Bidirectional control of autophagy by BECN1 BARA domain dynamics. *Mol. Cell* **73**, 339–353.e6 (2019).
15. X. Cheng *et al.*, Pacer mediates the function of class III PI3K and HOPS complexes in autophagosome maturation by engaging Stx17. *Mol. Cell* **65**, 1029–1043.e5 (2017).
16. Y.-M. Kim *et al.*, mTORC1 phosphorylates UVRAG to negatively regulate autophagosome and endosome maturation. *Mol. Cell* **57**, 207–218 (2015).
17. L. N. Young, K. Cho, R. Lawrence, R. Zoncu, J. H. Hurley, Dynamics and architecture of the NRBF2-containing phosphatidylinositol 3-kinase complex I of autophagy. *Proc. Natl. Acad. Sci. U.S.A.* **113**, 8224–8229 (2016).
18. C. Behrends, M. E. Sowa, S. P. Gygi, J. W. Harper, Network organization of the human autophagy system. *Nature* **466**, 68–76 (2010).
19. Y. Araki *et al.*, Atg38 is required for autophagy-specific phosphatidylinositol 3-kinase complex integrity. *J. Cell Biol.* **203**, 299–313 (2013).

20. Y. Cao *et al*., NRBF2 regulates macroautophagy as a component of VPS34 complex I. *Biochem. J.* **461**, 315–322 (2014).
21. J. Lu *et al*., NRBF2 regulates autophagy and prevents liver injury by modulating Atg14L-linked phosphatidylinositol-3 kinase III activity. *Nat. Commun.* **5**, 3920 (2014).
22. C. Yang *et al*., NRBF2 is involved in the autophagic degradation process of APP-CTFs in Alzheimer disease models. *Autophagy* **13**, 2028–2040 (2017).
23. X. Ma *et al*., MTORC1-mediated NRBF2 phosphorylation functions as a switch for the class III PtdIns3K and autophagy. *Autophagy* **13**, 592–607 (2017).
24. Y. Zhong *et al*., Nrbf2 protein suppresses autophagy by modulating Atg14L protein-containing Beclin 1-Vps34 complex architecture and reducing intracellular phosphatidylinositol-3 phosphate levels. *J. Biol. Chem.* **289**, 26021–26037 (2014).
25. Y. Ohashi *et al*., Characterization of Atg38 and NRBF2, a fifth subunit of the autophagic Vps34/PIK3C3 complex. *Autophagy* **12**, 2129–2144 (2016).
26. M. Ma *et al*., Cryo-EM structure and biochemical analysis reveal the basis of the functional difference between human PI3KC3-C1 and -C2. *Cell Res.* **27**, 989–1001 (2017).
27. G. Stjepanovic, S. Baskaran, M. G. Lin, J. H. Hurley, Vps34 kinase domain dynamics regulate the autophagic PI 3-kinase complex. *Mol. Cell* **67**, 528–534.e3 (2017).
28. C. Suloway *et al*., Automated molecular microscopy: The new Leginon system. *J. Struct. Biol.* **151**, 41–60 (2005).
29. S. Q. Zheng *et al*., MotionCor2: Anisotropic correction of beam-induced motion for improved cryo-electron microscopy. *Nat. Methods* **14**, 331–332 (2017).
30. S. H. W. Scheres, RELION: Implementation of a Bayesian approach to cryo-EM structure determination. *J. Struct. Biol.* **180**, 519–530 (2012).
31. A. Punjanji, J. L. Rubinstein, D. A. Fleet, M. A. Brubaker, cryoSPARC: Algorithms for rapid unsupervised cryo-EM structure determination. *Nat. Methods* **14**, 290–296 (2017).
32. K. Zhang, Gctf: Real-time CTF determination and correction. *J. Struct. Biol.* **193**, 1–12 (2016).
33. M. Schorb, I. Haberbosch, W. J. H. Hagen, Y. Schwab, D. N. Mastronarde, Software tools for automated transmission electron microscopy. *Nat. Methods* **16**, 471–477 (2019).
34. L. N. Young, F. Goerdeler, J. H. Hurley, NRBF2-MIT-linker-BECN1 containing PI3KC3-C1. Electron Microscopy Data Bank (EMDB). https://www.ebi.ac.uk/pdbe/entry/emdb/EMD-20387/volume. Deposited 29 June 2019.
35. L. N. Young, F. Goerdeler, J. H. Hurley, Activated Class III PI-3 Kinase by NRBF2. Electron Microscopy Data Bank (EMDB). https://www.ebi.ac.uk/pdbe/entry/emdb/EMD-20390/volume. Deposited 1 July 2019.